

Constraints on the structure of hot exozodiacal dust belts

Florian Kirchschräger^{1*}, Sebastian Wolf¹, Alexander V. Krivov², Harald Mutschke², and Robert Brunngräber¹

¹Kiel University, Institute of Theoretical Physics and Astrophysics, Leibnizstraße 15, 24118 Kiel, Germany

²Friedrich Schiller University Jena, Astrophysical Institute and University Observatory, Schillergäßchen 2-3, 07745 Jena, Germany

Accepted 2017 January 20. Received 2017 January 20; in original form 2016 July 18

ABSTRACT

Recent interferometric surveys of nearby main-sequence stars show a faint but significant near-infrared excess in roughly two dozen systems, i.e. around 10% to 30% of stars surveyed. This excess is attributed to dust located in the immediate vicinity of the star, the origin of which is highly debated. We used previously published interferometric observations to constrain the properties and distribution of this hot dust. Considering both scattered radiation and thermal reemission, we modelled the observed excess in nine of these systems. We find that grains have to be sufficiently absorbing to be consistent with the observed excess, while dielectric grains with pure silicate compositions fail to reproduce the observations. The dust should be located within $\sim 0.01 - 1$ au from the star depending on its luminosity. Furthermore, we find a significant trend for the disc radius to increase with the stellar luminosity. The dust grains are determined to be below $0.2 - 0.5 \mu\text{m}$, but above $0.02 - 0.15 \mu\text{m}$ in radius. The dust masses amount to $(0.2 - 3.5) \times 10^{-9} M_{\oplus}$. The near-infrared excess is probably dominated by thermal reemission, though a contribution of scattered light up to 35% cannot be completely excluded. The polarisation degree predicted by our models is always below 5%, and for grains smaller than $\sim 0.2 \mu\text{m}$ even below 1%. We also modelled the observed near-infrared excess of another ten systems with poorer data in the mid-infrared. The basic results for these systems appear qualitatively similar, yet the constraints on the dust location and the grain sizes are weaker.

Key words: (stars:) circumstellar matter – interplanetary medium – planets and satellites: fundamental parameters – zodiacal dust – infrared: planetary systems – techniques: interferometric

1 INTRODUCTION

The zodiacal dust cloud in the solar system has been studied intensively by in situ spacecraft measurements, remote observations at visible and infrared wavelengths, and theoretical modelling (e.g. Mann et al. 2004). Dust is present at all heliocentric distances, down to a few solar radii, where it is seen as the F-corona (e.g. Kimura & Mann 1998; Hahn et al. 2002). The total zodiacal dust mass has been estimated to $10^{-9} - 10^{-7} M_{\oplus}$ (Leinert 1996; Fixsen & Dwek 2002). For comparison, the dust mass of the Kuiper belt amounts to $(3 - 5) \times 10^{-7} M_{\oplus}$ (while the total mass in the Kuiper-belt objects is $\sim 0.12 M_{\oplus}$; Vitense et al. 2012). Most of the zodiacal dust is believed to originate from disintegration of short-period comets, with some contribution from asteroids (Nesvorný et al. 2010).

Zodiacal dust around stars other than the Sun, called

exozodiacal dust, was first detected around Vega by a deficit of the interferometric visibility compared to that expected from the star alone. Excluding close companions, stellar oblateness or gas emission, such a visibility deficit in the near-infrared (NIR) K waveband (Absil et al. 2006) is attributed to thermal reemission of hot dust or scattering of stellar radiation on these grains (e.g. Akeson et al. 2009; De-frère et al. 2011; Roberge et al. 2012). So far, an exozodiacal dust environment has been detected through a signature in the NIR around about two dozens of main-sequence stars (Absil et al. 2009, 2013; Ertel et al. 2014).

The exozodis have been inferred to be by about three order of magnitude brighter than the zodiacal cloud in the solar system. In contrast to the solar system’s zodiacal cloud, their origin remains unclear. Also unclear are the mechanisms that sustain the exozodiacal dust at the observed level. Poynting-Robertson effect, stellar radiation blow-out, and grain collisions are only a small selection of processes which should remove the dust and disperse the disc within a few

* E-mail: kirchschrager@astrophysik.uni-kiel.de

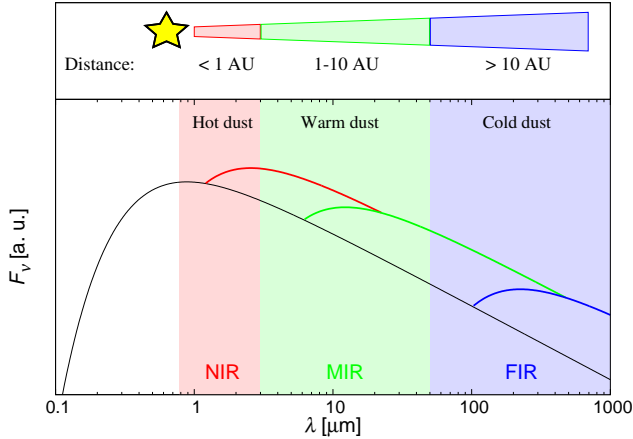


Figure 1. Illustration of so-called hot, warm, and cold dust traced through their contributions to different parts of the SED. The stellar photosphere (black solid line) corresponds to a solar type star ($T_{\star} = 5777$ K). The height of the excess curves is arbitrary.

million years (e. g. Wyatt 2008; Krivov 2010; Matthews et al. 2014). At small distances to the star, dispersal mechanisms have particularly short time scales, making the presence of exozodiacal dust at old ages a conundrum (e. g. Rieke et al. 2005).

Compared to cold dust located in Kuiper belt analogues at radii larger than 10 au, causing an excess in the mid-(MIR) and far-infrared (FIR) wavelength range, NIR observations trace the disc region within or around 1–10 au from the central star (see Fig. 1). Thus studies of exozodis offer a way to better understand the inner regions of extrasolar planetary systems. Besides, the possible presence of small grains in exozodiacal clouds is a potential problem for the detection of terrestrial planets in the habitable zone of these systems (e. g. Agol 2007; Beckwith 2008). This provides another motivation to study the exozodiacal dust and its properties.

Previously published constraints favour discs consisting of small particles in a narrow ring around the star (e. g. Rieke et al. 2016). The dust has to be located beyond the sublimation radius of the grains, which typically amounts to a few solar radii (Mann et al. 2004). For Vega, Fomalhaut, and β Leo, small refractory particles ($\sim 10 - 500$ nm) at distances of $\sim 0.1 - 0.3$ au in narrow rings are required to account for the hot excess (Absil et al. 2006; Akeson et al. 2009; Defrère et al. 2011; Lebreton et al. 2013). Rieke et al. (2016) obtained similar results, constraining the maximum grain size to ~ 200 nm.

Due to the proximity to the star, spatially resolved direct imaging observations of the exozodiacal dust hosting environments are missing. Although Rieke et al. (2016) found a weakly but significantly bluer photometric colour for these systems compared to stars without exozodiacal dust, the detection of these systems was only possible so far through interferometric observations. The observing strategy is to measure the visibility using a suitable set of baseline configurations. A significant deficit of the interferometric visibility at low spatial frequencies indicates the presence of dust material spatially resolved and beyond their sublimation distance, enabling direct determination of the flux ratio between disc and central star (Di Folco et al. 2004). Two

interferometric surveys using CHARA/FLUOR (Absil et al. 2013) and VLTI/PIONIER (Ertel et al. 2014) resulted in detections of exozodiacal dust around main-sequence stars with an incidence rate of 10 % to 30 %.

Based on the observational data available, we intend to put stronger constraints on the exozodiacal dust distribution than those that were derived previously. For this purpose, in this paper we model selected NIR to FIR observations of systems for which NIR long-baseline interferometric observations indicate the presence of hot dust close to the star. Our sample of systems and the methods we use to analyse their observations are described in Sect. 2. The results are presented in Section 3. A discussion of possible mechanisms that may create and sustain the exozodiacal dust is given in Section 4. Section 5 summarises our findings.

2 ANALYSIS

In this section we present both our selection of systems and the methods we use to constrain the parameters of the spatial distribution of the dust and the sizes of the dust grains. The survey of stars with hot exozodiacal dust is introduced in Section 2.1 and the disc and dust model are described in Section 2.2. The procedure and the observational data applied to constrain the model parameters are presented in Section 2.3 and 2.4, and the calculation of the sublimation radius is described in Section 2.5. A discussion of the impact of the limited spatial resolution of the NIR and MIR observations is given in Section 2.6.

2.1 Survey of stars with NIR excess

In Table 1 those systems of the surveys of Absil et al. (2013) in K band and Ertel et al. (2014) in H band are compiled which show a significant NIR excess that is indicative of hot exozodiacal dust. In addition, HD 216956 (Fomalhaut) is included, which was observed with VLTI/VINCI in K band (Absil et al. 2009). Stars for which a detected NIR excess can be attributed to a different mechanism or a companion (Mawet et al. 2011; Absil et al. 2013; Bonsor et al. 2013a; Marion et al. 2014) have been excluded from this study. Besides HD 7788 (κ Tuc), for which a temporal variability of the excess was detected (Ertel et al. 2016), the list of known systems with hot exozodiacal dust is complete. Ertel et al. (2016) also found a tentative indication for a temporal variability of the excess of HD 210302 (τ PsA). However, since this variability is not significant, the system is considered in our study. All of the listed stars are at or close to the main sequence, with spectral classes ranging from A0 to G8 and luminosities from $L_{\star} \sim 0.4 L_{\odot}$ to $\sim 40 L_{\odot}$.

To derive the flux of the NIR excess from the observed visibilities, uniformly bright emission was adopted in the whole field of view (Di Folco et al. 2004). We divide the selected systems in two groups: Group I comprises all systems with interferometric flux measurements at $\lambda = 8.5 \mu\text{m}$ which will help to find strong constraints for the disc model. Group II contains all systems without such observations at $\lambda = 8.5 \mu\text{m}$. As we will see in Section 3.4, the dust parameters in these systems cannot be constrained as tightly as for the Group I-targets.

Table 1. Parameters of targets with NIR excess (Absil et al. 2009; Absil et al. 2013; Ertel et al. 2014) which is attributed to circumstellar dust. Group I/Group II comprises all systems with/without interferometric observations at $\lambda = 8.5 \mu\text{m}$ (Mennesson et al. 2014).

Notes to the IR-excesses: “H” excess in the H band; “K” excess in the K band; “(K)” observed in K band, but without information on the excess (Defrère et al. 2012); “/” no interferometric observation; “-” no significant excess detected; “(+)” excess uncertain, discussed differently in literature, SED makes no clear statement; “+” weak significant excess; “++” strong significant excess

HD number	HIP number	Alter. name	d [pc]	T_* [K]	L_* [L_\odot]	Spectral class	Age [Gyr]	NIR excess	8.5 μm excess	24 μm excess	70 μm excess	Ref. excess
Group I												
10700	8102	τ Cet	3.7	5290	0.46	G8 V	10	K	-	-	+	(a), (b), (c), (d)
22484	16852	10 Tau	13.7	5998	3.06	F9 IV-V	6.7	K	-	-	+	(d), (e), (f)
56537	35350	λ Gem	28.9	7932	27.4	A3 V	0.5	K	-	-	-	(d), (g), (h)
102647	57632	β Leo	11.1	8604	13.25	A3 V	0.1	K	+	+	++	(d), (i)
172167	91262	α Lyr	7.8	9620	37	A0 V	0.7	H, K	-	-	++	(d), (i), (j), (k)
177724	93747	ζ Aql	25.5	9078	36.56	A0 IV-V	0.8	K	-	-	-	(d), (l), (m)
187642	97649	α Aql	5.1	7680	10.2	A7 IV-V	1.3	K	-	-	-	(c), (d), (g), (n)
203280	105199	α Cep	15.0	7700	19.97	A7 IV-V	0.8	K	-	-	-	(d), (l)
216956	113368	α PsA	7.7	8590	16.6	A3 V	0.4	K	-	+	++	(d), (o), (p), (q)
Group II												
2262	2072	κ Phe	23.5	9506	16	A5 IV	0.7	H	/	+	+	(i)
14412	10798		12.7	5371	0.38	G8 V	3.7	H	/	-	-	(f)
20794	15510	e Eri	6.1	5401	0.66	G8 V	8.1	H	/	(+)	(+)	(r), (s)
28355	20901	b Tau	49.2	7852	16	A7 V	0.7	H	/	+	++	(i)
39060	27321	β Pic	19.3	8203	13	A6 V	0.02	H, (K)	/	++	++	(i)
104731	58803		24.2	6651	4	F5 V	1.6	H	/	-	-	(f)
108767	60965	δ Crv	26.9	10209	40	A0 IV	0.3	H	/	-	-	(i)
131156	72659	ξ Boo	6.5	5483	0.6	G7 V	0.3	K	/	-	-	(g)
173667	92043	110 Her	19.1	6296	6.01	F5.5 IV-V	3.4	K	/	-	(+)	(e), (s)
210302	109422	τ PsA	18.7	6339	2.5	F6 V	2.2	H	/	-	-	(e), (f)

References: (a) Greaves et al. (2004); (b) Chen et al. (2006); (c) Habing et al. (2001); (d) Mennesson et al. (2014); (e) Kóspál et al. (2009); (f) Trilling et al. (2008); (g) Gáspár et al. (2013); (h) Chen et al. (2014); (i) Su et al. (2006); (j) Gillett (1986); (k) Defrère et al. (2011); (l) Chen et al. (2005); (m) Plavchan et al. (2009); (n) Rieke et al. (2005); (o) Stapelfeldt et al. (2004); (p) Su et al. (2013); (q) Acke et al. (2012); (r) Wyatt et al. (2012); (s) Beichman et al. (2006). The distances are derived from parallax measurements (van Leeuwen 2007). Stellar temperatures and luminosities are adopted from (c), van Belle et al. (2001), van Belle et al. (2006), Wyatt et al. (2007b), Müller et al. (2010), Pepe et al. (2011), Zorec & Royer (2012), Boyajian et al. (2013), and Pace (2013), spectral classes and stellar ages are taken from Mamajek (2012), Vican (2012), Absil et al. (2013), Ertel et al. (2014), and Mamajek & Bell (2014).

2.2 Model description

The aim of the study is to fit the NIR fluxes of the hot exozodiacal dust systems. Owing to a paucity of observational data, a simple disc model is adopted to keep the number of free parameters small.

Disc properties. The disc model represents a thin ring with an inner radius R and outer radius $R_{\text{out}} = 1.5 R$. The number density decreases with $n(r) \propto r^{-1}$. The dust mass M_{dust} is chosen as a scaling factor to match the NIR flux for each individual system. Taking into account scattered radiation, the inclination i of the disc has to be considered. We examine three cases: a face-on ($i = 0^\circ$) and an edge-on disc ($i = 90^\circ$) with an half opening angle of 5° , and a spherical shell around the central star. The latter case is motivated by the scenario of dust expelled from exo-Oort cloud comets, or by stellar magnetic fields which compel charged dust grains on orbits perpendicular to the disc plane.

Dust properties. Each dust ring is composed of compact and spherical dust grains with a single grain radius a . The grains are assumed to consist of pure graphite ($\rho = 2.24 \text{ g cm}^{-3}$; Weingartner & Draine 2001), using the $1/3-2/3$ approximation (Draine & Malhotra 1993).

The optical properties of the grains are calculated with the software tool `miex` which is based on the theory of Mie-scattering (Mie 1908; Wolf & Voshchinnikov 2004). Single

Table 2. Parameter space for modelling the systems from Tab. 1.

Parameter	Range	Number	Grid
Disc ring radius R [au]	0.01 – 10	100	log.
Grain size a [μm]	0.001 – 10/100	100	log.
Inclination i	$0^\circ, 90^\circ$, sphere	3	discr.

scattering and reemission simulations are performed and the SEDs are calculated using an enhanced version of the tool `debris` (Ertel et al. 2011). All free parameters and the range within which they have been varied are presented in Table 2.

2.3 Procedure

To illustrate the data modelling procedure, the SED of the NIR excess harbouring system HD 56537 is shown in Figure 2. Obviously, many appropriate parameter settings exist which would allow one to reproduce the NIR excess. Fortunately, there exist further observations which potentially help to constrain the possible ranges for the grain size a and the disc ring radius R . In particular, the observed MIR and FIR fluxes provide strict upper limits on the total mass (for given dust properties and radial density distribution). Furthermore, an underestimation of the observed MIR and

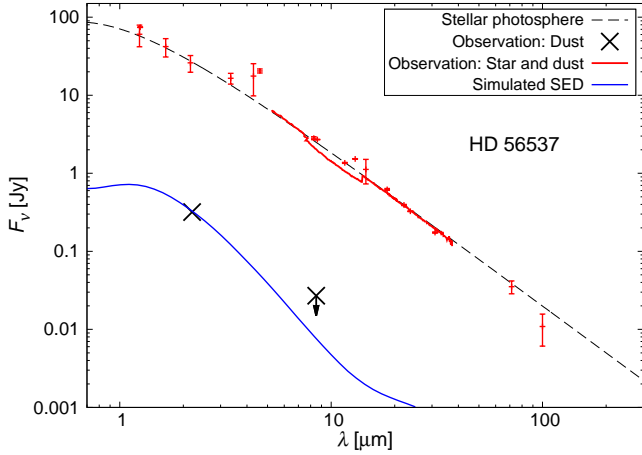


Figure 2. SED of HD 56537. The dashed line represents the stellar photosphere ($T_{\star} = 7932$ K, $L_{\star} = 27.4 L_{\odot}$), the red points show the observed fluxes (star plus dust, including Spitzer/IRIS spectrum; *VizieR*-catalogue) and the black points mark the excess of the dust (without stellar flux contribution). The flux at $\lambda = 8.5 \mu\text{m}$ is an upper limit. A simulated SED which reproduces the NIR flux without overestimating the observed fluxes in the MIR and FIR is shown as the blue solid line.

FIR fluxes would still be in agreement with the observations because of the potential presence of additional dust distributions located at larger distances to the star, similar to the Kuiper belt in the solar system.

The ratio of the simulated flux in the NIR to the simulated flux in the MIR and FIR is determined for each parameter setting:

$$S_{\lambda_{\text{MIR/FIR}}}^{\text{simu}} = \frac{F_{\nu}^{\text{simu}}(\lambda_{\text{NIR}})}{F_{\nu}^{\text{simu}}(\lambda_{\text{MIR/FIR}})}. \quad (1)$$

The simulated colour $S_{\lambda_{\text{MIR/FIR}}}^{\text{simu}}$ has to be compared to the observed colour,

$$S_{\lambda_{\text{MIR/FIR}}}^{\text{obs}} = \frac{F_{\nu}^{\text{obs}}(\lambda_{\text{NIR}})}{F_{\nu}^{\text{obs}}(\lambda_{\text{MIR/FIR}})}, \quad (2)$$

and must fulfill the condition

$$S_{\lambda_{\text{MIR/FIR}}}^{\text{simu}} \geq S_{\lambda_{\text{MIR/FIR}}}^{\text{obs}} \quad (3)$$

in order to reproduce the NIR excess. In this study we assume that the hot dust emission does not vary with time (see Sect. 3.6 for a discussion of the time variability of the NIR excess).

2.4 Observational data

2.4.1 NIR data

Except for HD 216956 (Fomalhaut), the NIR fluxes of the dust around all Group I-targets as well as HD 131156 and HD 173667 of Group II are determined by FLUOR/CHARA (Absil et al. 2013). The data for HD 216956 are taken with VLTI/VINCI (Absil et al. 2009), while HD 14412, HD 104731 and HD 108767 of Group II are observed with VLTI/PIONIER (Ertel et al. 2014). For the remaining targets of Group II, the weighted mean flux ratios of Ertel et al. (2014, 2016) are used (PIONIER).

2.4.2 MIR and FIR data

The colours (Eq. 1) are analysed for the wavelengths $\lambda = 24 \mu\text{m}$ and $70 \mu\text{m}$ for all Group I and II-targets. Table 1 indicates which of the systems show a significant excess in the MIR or FIR. Several systems have no or only minor excess at these wavelengths. To cope with the problem that a determination of the flux emitted by the dust is affected mainly by the uncertainty of the stellar photospheric flux, we use the measured flux which comprises the contribution of both dust and stellar photosphere at $\lambda_{\text{MIR/FIR}} = 24 \mu\text{m}$ and $70 \mu\text{m}$. Although this condition is weaker than Eq. (3), this helps to circumvent the uncertainty of the photospheric flux.

For HD 10700, we use IRAS-fluxes at $60 \mu\text{m}$ and $100 \mu\text{m}$ (Greaves et al. 2004) to interpolate the excess flux at $\lambda = 70 \mu\text{m}$ since there exists no observation at this wavelength. For HD 131156 and HD 187642, both fluxes at $24 \mu\text{m}$ and $70 \mu\text{m}$ are estimated from the stellar photosphere and interpolation of observations of IRAS (Habing et al. 2001), Akari, WISE, and Herschel/PACS at $100 \mu\text{m}$ (Gáspár et al. 2013).

In addition, we use MIR data from Keck for the Group I-targets (Mennesson et al. 2014). For each of these systems we calculate the flux emitted from the dust at $\lambda = 8.5 \mu\text{m}$ using $F_{\text{dust}} \sim 2.5 F_{\star} E_{8-9}$ (B. Mennesson, private communication), where E_{8-9} is the measured excess leak given in their Table 2. The factor 2.5 corresponds to the average transmission value over the region extending from the inner and outer working angle. Only one system (HD 102647) shows a significant excess. For all the other systems we use the significance limit as an upper limit for the flux at $\lambda = 8.5 \mu\text{m}$.

2.5 Sublimation radius and habitable zone

Dust sublimation in the vicinity of the star sets the minimum distance at which the dust material can be located. Subsequently to the investigation of the parameter space presented in Section 2.2, we determine the sublimation radii as a function of grain size a in thermal equilibrium. The sublimation radius R_{sub} of a particle with a sublimation temperature T_{sub} amounts to

$$R_{\text{sub}} = \frac{R_{\star}}{2} \sqrt{\frac{\int_0^{\infty} B_{\lambda}(T_{\star}) Q_{\text{abs}}(a, \lambda) d\lambda}{\int_0^{\infty} B_{\lambda}(T_{\text{sub}}) Q_{\text{abs}}(a, \lambda) d\lambda}}, \quad (4)$$

(Backman & Paresce 1993), where B_{λ} is the Planck function and Q_{abs} is the dimensionless absorption efficiency. We assume a sublimation temperature of $T_{\text{sub}} = 2000$ K (e.g. Lamoreaux et al. 1987) for graphite and determine the sublimation radius for each system. It should be noted that the modelling results presented in Section 3 strongly depend on the exact choice of the sublimation temperature T_{sub} .

For an approximate estimation of the borders of the habitable zone we assume a temperature profile

$$T_{\text{HZ}} = (278.3 \text{ K}) \left(\frac{L_{\star}}{L_{\odot}} \right)^{0.25} \left(\frac{1 \text{ au}}{R_{\text{HZ}}} \right)^{0.5}, \quad (5)$$

where T_{HZ} is the temperature at the radial distance R_{HZ} of the habitable zone. The temperature range is 210 to 320 K, equivalent to the habitable zone location in the solar system (e.g. Kopparapu et al. 2013).

2.6 Spatially resolved dust emission and sensitivity dependency over the field of view

The circumstellar emission in the NIR is spatially resolved. However, dust within an inner working angle θ does not contribute to the NIR excess, which has to be considered in the modelling.

The angular resolution of an interferometer is given by

$$\theta = \lambda / (x B), \quad (6)$$

where B is the projected baseline and $x \in \{1, 2, 4, \dots\}$. Since the correct value for x is contentious, we choose a different approach. We assume a uniformly bright emission ring (face-on)¹ with an inner radius R and outer radius $R_{\text{out}} = 1.5 R$ and adopt the measured NIR flux ratio $f_{\text{observation}}$ of the spatially resolved dust and the central star. By varying the inner radius, we calculate the visibility function $V_{(\star + \text{disc})}$ of the star in combination with the disc for this simplified system. Subsequently, the ratio f' of the simulated observational date is derived via $f' = (V_{\star} - V_{(\star + \text{disc})}) / V_{\star}$, where V_{\star} denotes the stellar visibility alone (Di Folco et al. 2004).

For large inner radii (*right* in Figure 3), the entire disc is spatially resolved, and the derived ratio f' equals the given ratio $f_{\text{observation}}$. Decreasing the inner radius, the emission gets less resolved, resulting in a modulation of f' and an increase of the difference between f' and $f_{\text{observation}}$. For small inner radii (Fig. 3, *left*), the entire disc is unresolved and f' converges to 0. We define the inner working angle of the simulated NIR observation as the smallest value θ for which the derived ratio f' is still within the interval $f_{\text{observation}} \pm \sigma_f$, where σ_f is the uncertainty of the real NIR observation. This is the most conservative approach for the adoption of an inner working angle, since we want to avoid assuming a too large inner working angle and thus constraining the dust distribution in a wrong way. For the FLUOR observation of the system HD 56537 in Figure 3, a value of $\theta = 0.0034$ as is derived. Using Eq. 6, this is equivalent to $x = 3.97$. For comparison, Absil et al. (2013) assumed a value of 4 when examining the resolution of the sublimation radius. In our study, x is between 3.4 and 4.1 for all observations with FLUOR, PIONIER and VINCI of the systems in Table 1. The small variability in x is the result of the uncertainty σ_f of the individual observations.

Additionally to the interferometric data in the NIR, MIR nulling data obtained with the Keck Interferometer are used for the Group I-targets. The inner working angle for these observations is 6 mas (Mennesson et al. 2014). The signal for sources at projected separations larger than 200 mas is strongly attenuated or even completely missed, setting an outer working angle of the instrument.

After the determination of the inner working angle for each system and NIR and MIR observation, it is used as a strong limiting condition for the simulations: radiation which is scattered or reemitted within the inner working angle (or outside the outer working angle) is completely neglected. While in the face-on case only discs with small inner radii R are affected, a significant fraction of radiation

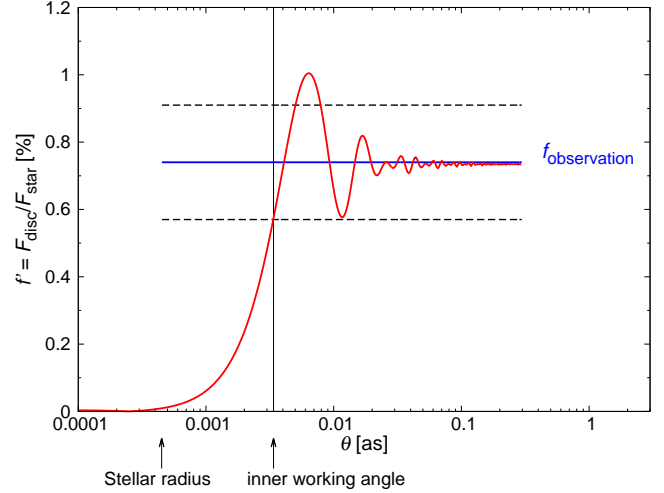


Figure 3. Ratio $f' = F_{\text{disc}} / F_{\star}$ for the system HD 56537, derived from the simulated visibility function of a uniformly bright emission ring (face-on) for different inner radii R (see Sect. 2.6 for details). The inner working angle of the simulated NIR observation is defined as the smallest value θ for which the ratio f' is still within the interval $f_{\text{observation}} \pm \sigma_f$, where σ_f is the uncertainty of the real NIR observation.

is never resolved by the case of edge-on discs and spherical dust shells. In particular, a strong forward-scattering peak is invisible if scattered light is considered.

In addition to the inner working angle, the sensitivity of an optical, single mode fiber interferometer such as FLUOR, PIONIER, or VINCI is not uniform over the field of view. Instead, it can be approximated as a Gaussian function with a FWHM of 0.8 as, 0.4 as, and 1.6 as, respectively (Absil et al. 2013; Ertel et al. 2014; Absil et al. 2009). This disparity is taken into account in our NIR simulations, so that emission further away from the star is weaker than emission closer in.

3 RESULTS

In this section the results of the disc modelling process are presented. For each parameter setting in Table 2 the colour $S_{\lambda_{\text{MIR/FIR}}}^{\text{simu}}$ is calculated and compared to $S_{\lambda_{\text{MIR/FIR}}}^{\text{obs}}$. At first we demonstrate the key results of the modelling for the exozodiacal dust system HD 56537 as a representative of Group I in detail (Sect. 3.1). Subsequently, we discuss the entire samples of Group I and II (Sect. 3.2 - 3.4). In Section 3.5 - 3.7 the uncertainty and the time variability of the NIR excess as well as constraints by spectrally dispersed data are discussed.

3.1 HD 56537

HD 56537 (λ Gem) is a 5×10^8 year old system (Vican 2012) with a significant K band excess ($0.74\% \pm 0.17\%$ of the stellar flux), but with no significant excess at $\lambda = 8.5 \mu\text{m}$, $24 \mu\text{m}$ or $70 \mu\text{m}$. This suggests that the NIR excess stems solely from the hot exozodiacal dust, with no contribution from other potential disc components. The results of the modelling are shown in Figure 4. Each panel represents a selected range of the parameter space consisting of the grain

¹ Similarly, a uniformly bright emission is also adopted in the whole field of view by Absil et al. (2009), Absil et al. (2013) and Ertel et al. (2014) to derive the NIR flux of the dust from the observations.

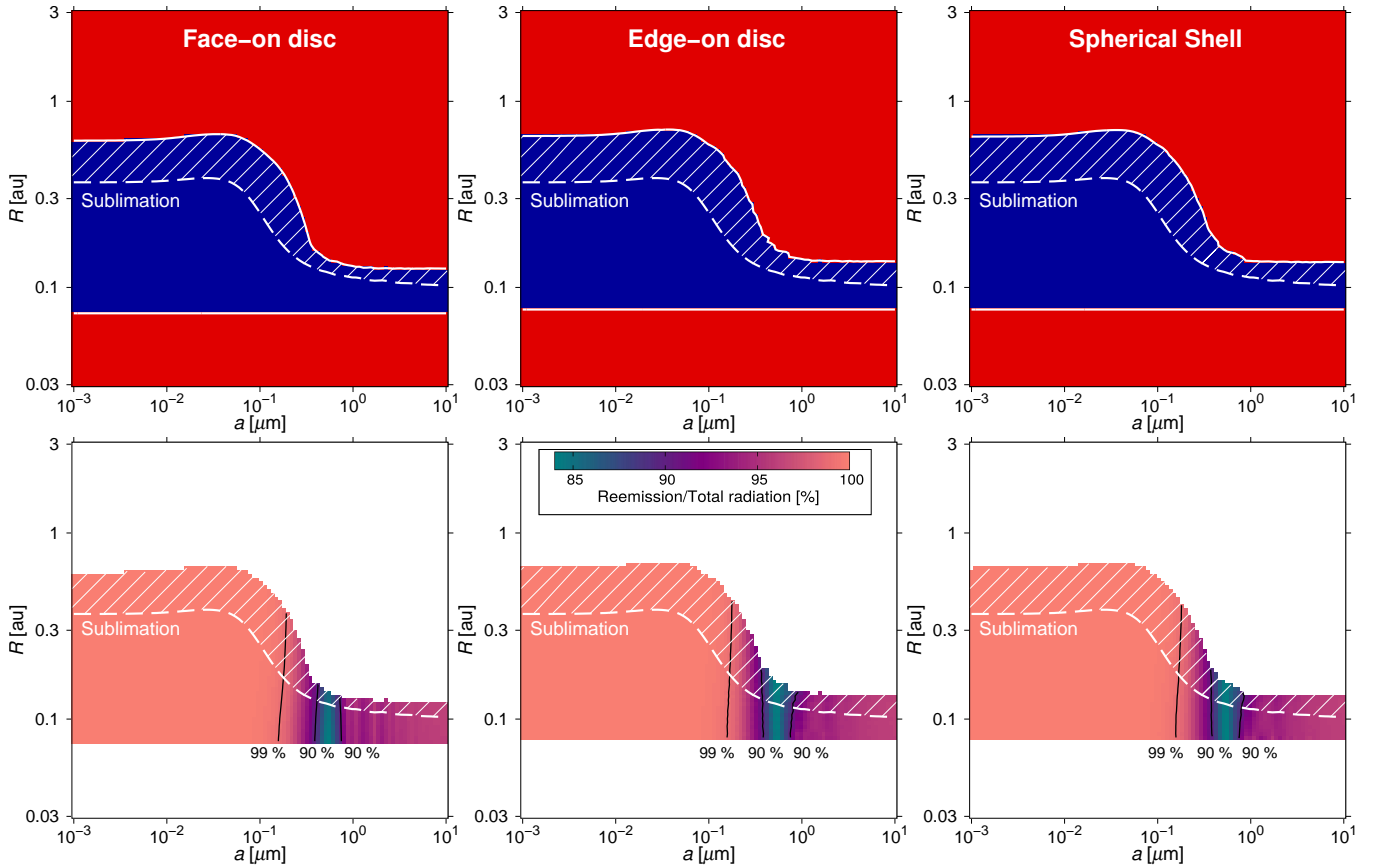


Figure 4. Explored parameter space for the system HD 56537. The dust material is pure graphite. The disc inclination is $i = 0^\circ$ (left column) and 90° (middle column), and the results for the case of a spherical dust distribution are shown in the right column. In the first row the calculations considering the observations at $\lambda = 2.2 \mu\text{m}$, $8.5 \mu\text{m}$, $24 \mu\text{m}$ and $70 \mu\text{m}$ are shown. The blue regions in the panels correspond to parameter settings which can reproduce the observational data, while the parameter settings of the red regions fail. The sublimation radius (white dashed line) and the upper blue-red border comprise the region of suitable parameter settings (dashed area). In the second row the ratio of the reemission to the total radiation is illustrated. The colour scale is linear, ranging from 84 % (turquoise) up to 100 % (apricot). Black contour lines show the 90 % and 99 % level.

size a and the dust ring radius R . In the following, we investigate potential constraints which can be derived for these quantities and determine the contribution of scattered and polarised radiation of the NIR flux.

3.1.1 Constraints on grain size and dust location

The results for different disc inclinations ($i = 0^\circ$ or 90°) and for the spherical dust shell are presented in Figure 4. Small differences between these three optically thin cases exist which are due to the dependence of the scattered NIR and MIR radiation on the light scattering geometry. In addition, the fraction of radiation from dust close to the star (which does not contribute to the observed flux) as well as the fraction of radiation from dust located further away (which does not change the observed flux either, due to the sensitivity of the optical single mode fiber) depend on the dust distribution geometry. The results for the spherical shell can be interpreted qualitatively as intermediate between the results for the face-on and the edge-on disc.

In the upper row of Figure 4 the calculations considering the observations at the wavelengths $\lambda = 8.5 \mu\text{m}$, $24 \mu\text{m}$ and $70 \mu\text{m}$ are shown. In the blue-coloured regions

the corresponding parameter settings reproduce the NIR excess without overestimating the fluxes at these three wavelengths, while in the red-coloured regions the simulated fluxes of at least one of them is too large. Models with inner radii $R \lesssim 0.08 \text{ au}$ fail because of the inner working angle of the simulated NIR observations. On the other hand, models with inner radii $0.08 \text{ au} \lesssim R \lesssim 0.14 \text{ au}$ reproduce the observations because of the larger inner working angle of the simulated MIR observations. Since the sublimation radius is spatially resolved by the NIR observations for all grain sizes, it depicts the minimum limit for the inner radius R (0.1 au). Furthermore, sublimation radius and the upper blue-red border comprise the region of the suitable parameter settings (dashed area). This area in the parameter space is evaluated for each system and the corresponding parameters for minimum and maximum dust ring radius, grain size, and mass are derived. For HD 56537, the maximum disc ring radius is $R_{\text{max}} = 0.65 \text{ au}$ (0.68 au; 0.68 au) for the face-on disc (edge-on disc; sphere). The total dust mass required to reproduce the NIR flux is between $0.5 \times 10^{-9} M_\oplus$ ($0.9 \times 10^{-9} M_\oplus$; $0.6 \times 10^{-9} M_\oplus$) and $22 \times 10^{-9} M_\oplus$ ($52 \times 10^{-9} M_\oplus$; $33 \times 10^{-9} M_\oplus$). The grain sizes for this system are not limited by our study, and both

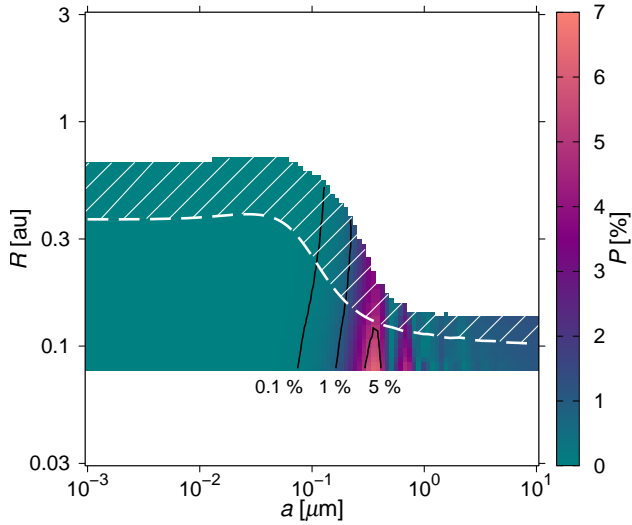


Figure 5. Polarisation degree P of the total radiation for the system HD 56537. The dashed white line indicates the sublimation radius and the region of suitable parameter settings is highlighted as dashed area (see Fig. 4). The black contour lines show the 0.1%, 1% and 5% level. The dust material is graphite and the inclination is 90° .

nanometer-sized grains and those larger than $\sim 10 \mu\text{m}$ can reproduce the observed excesses. The reason for the possible presence of the large particles is that the sublimation radius of this system is not spatially resolved by the MIR observation at $\lambda = 8.5 \mu\text{m}$. A pile-up of large grains near the sublimation radius would cause a detectable excess in the NIR, which could not be observed by the MIR observations. In contrast, the theoretical approach of an infinitely small resolution of both the NIR or MIR observations would rule out large grains in this system due to small observed fluxes at $\lambda = 8.5 \mu\text{m}$ compared to the NIR.

In general, a higher sublimation temperature would decrease the minimum radius and minimum dust mass and increase the maximum grain size.

3.1.2 Scattered and polarised radiation

The contribution of scattered radiation to the NIR flux is still an open question, although previously published studies tended to favour a small contribution (e. g. [van Lieshout et al. 2014](#); [Rieke et al. 2016](#)). The ratio of the thermal re-emission radiation to the total radiation is illustrated in the *second row* of Figure 4. We find that for suitable parameter settings thermal re-emission is the dominating source. The lowest ratio of the thermal re-emission to the total radiation for all three disc geometries amounts to 84%. For grain radii below $0.2 \mu\text{m}$ the ratio is larger than 99%. Consequently, the contribution of scattered radiation and thus the influence of the disc inclination are negligible for these small grains. Only for grains with radii between $0.2 \mu\text{m}$ and $\sim 1 \mu\text{m}$, the fraction of scattered radiation is larger.

Moreover, the polarisation degree P of the total radiation in the NIR is determined (Fig. 5). According to the low contribution of scattered radiation for the suitable parameter settings, the polarisation degree is below 5% and

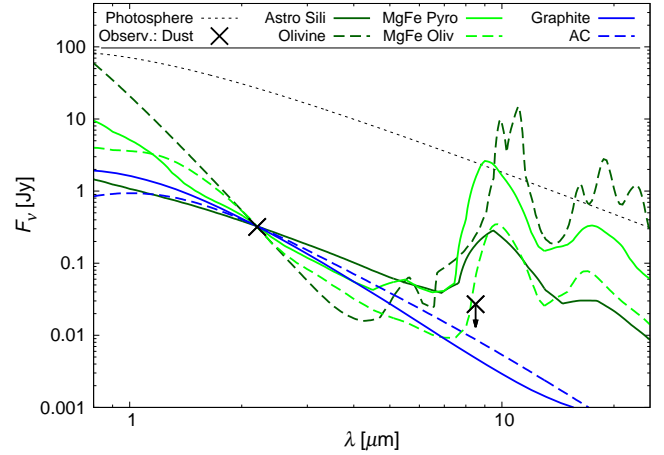


Figure 6. SED considering different dust materials (see text) in a disc with ring radius $R = 0.4 \text{ au}$ and dust grains of size $a = 0.1 \mu\text{m}$ around HD 56537. The dust mass M_{dust} is chosen as a scaling factor to match the flux at $\lambda = 2.2 \mu\text{m}$ for each material. All silicates (green) show the characteristic spectral feature around $\lambda \sim 10 \mu\text{m}$ which causes an overestimation of the flux at $8.5 \mu\text{m}$, contrary to the observations. In contrast, carbonaceous grains (blue) reproduce the observations.

even below 1% for grains smaller than $0.24 \mu\text{m}$. Only for grain radii between $0.3 \mu\text{m}$ and $\sim 0.5 \mu\text{m}$, the polarisation is larger than 2%. Because of symmetry constraints, the integrated polarisation equals zero in the case of the face-on disc and the spherical shell. The results are consistent with polarisation measurements of hot dust stars with the instrument HIPPI at the Anglo-Australian Telescope in the optical wavelength range, which have shown that the detected polarised emission does not exceed 1% ([Marshall et al. 2016](#)).

3.1.3 Different dust materials

To investigate the impact of different dust materials on the disc modelling, appropriate simulations of the SED are performed for an exemplary disc with ring radius $R = 0.4 \text{ au}$ and dust grains of size $a = 0.1 \mu\text{m}$ (Fig. 6). Besides graphite (optical data from [Weingartner & Draine 2001](#)) from the previous section, we also consider:

- Astronomical silicate (*Astro Sili*; [Weingartner & Draine 2001](#)),
- Natural (terrestrial) olivine from San Carlos, Arizona (*Olivine*; data for 928 K; [Zeidler et al. 2011, 2015](#)),
- Glassy magnesium-iron silicates with pyroxene composition, $\text{Mg}_{0.5}\text{Fe}_{0.5}\text{SiO}_3$ (*MgFe Pyro*; [Dorschner et al. 1995](#)),
- Glassy magnesium-iron silicates with olivine composition, MgFe SiO_4 (*MgFe Oliv*; [Dorschner et al. 1995](#)),
- Amorphous carbonaceous dust analogues produced by pyrolysis of cellulose at 1000°C (*AC*; [Jäger et al. 1998](#)).

The first four materials are silicates and the last one is a carbon. The silicates show the characteristic broad spectral feature around $\lambda \sim 10 \mu\text{m}$. Regarding the thermal re-emission as the dominating source of radiation, the flux at $\lambda = 8.5 \mu\text{m}$ is expected to be larger than the NIR flux in most cases. However, the flux observed at $\lambda = 8.5 \mu\text{m}$ in systems with

hot exozodiacal dust is one order of magnitude below the measured NIR flux. We cannot reproduce the observational constraints under the assumption of dust grains consisting of any of the considered silicates. More specifically, only disc ring radii below the sublimation radius in combination with the dominance of large grains (where the spectral feature is less pronounced) would result in fluxes which are in agreement with the observations. Although the modelling cannot exclude the presence of large particles due to the limited resolution of the observation at $\lambda = 8.5 \mu\text{m}$, we expect that they do not occur in the disc. Therefore, large amounts of silicates in the material of the exozodiacal dust are excluded.

In contrast, the crystalline graphite and the amorphous carbon can reproduce the observations, so that we focus on graphite in the following sections.

3.2 Survey: Group I-targets

We now perform the calculations of the SED for each target of Group I and determine the parameter settings which reproduce the observational data. The results are shown in Figure 7.

The minimum disc ring radius R_{\min} varies between ~ 0.01 au and ~ 0.2 au and increases in a rough trend with the stellar luminosity. This is of course expected, since R_{\min} is in most cases determined by the sublimation radius R_{sub} .

The maximum disc ring radius R_{\max} is below ~ 1 au for all systems, with a minimum value of 0.06 au for HD 10700. Interestingly, it also appears to increase with the stellar luminosity. In contrast to the minimum radius, this trend is not obvious, since we do not know which physical processes set the location of the exozodiacal dust and whether or not these are, for instance, temperature-dependent. Accordingly, a tentative trend might be important, and we now undertake a basic statistical analysis.

The Pearson correlation coefficient between $\log L_*$ and $\log R_{\max}$ amounts to $R_p = 0.70$, and the Spearman rank correlation coefficient, which is more robust and does not require linearity, is $R_s = 0.65$. If two apparent outliers, HD 22484 and HD 102647, are dropped from the analysis, the correlation gets even stronger ($R_p = 0.85$, $R_s = 0.94$), indicating a high significance.

Since the trend is significant, we can make a power-law fit. The result strongly depends on how we treat the outliers (Fig. 8). For the full sample of nine stars, i.e. not excluding any outliers, the result is $R_{\max} \propto L_*^{0.5 \pm 0.3}$. Without two obvious outliers mentioned above we find $R_{\max} \propto L_*^{1.4 \pm 0.4}$. Figure 8 suggests that HD 172167 (Vega) may be another outlier. Excluding all three systems results in $R_{\max} \propto L_*^{1.8 \pm 0.2}$. Trying to understand which of these relations can be more trustable, we can look at all three potential outliers. Indeed, HD 22484 has the relatively small ratio of the measured NIR flux to the flux at $8.5 \mu\text{m}$, which results in weaker constraints for the model parameters (see Sect. 3.3). Thus we deem discarding this system reasonable. HD 102647 (β Leo) is the only system with a significantly high flux at $8.5 \mu\text{m}$, and this system reveals some differences to other resolved cases (see notes on this system in Sect. 3.3). As for Vega, there is some uncertainty about its luminosity (see Sect. 3.3 for this star, too). Yet we do not see any justifiable reason for excluding β Leo and Vega from the analysis. Discarding

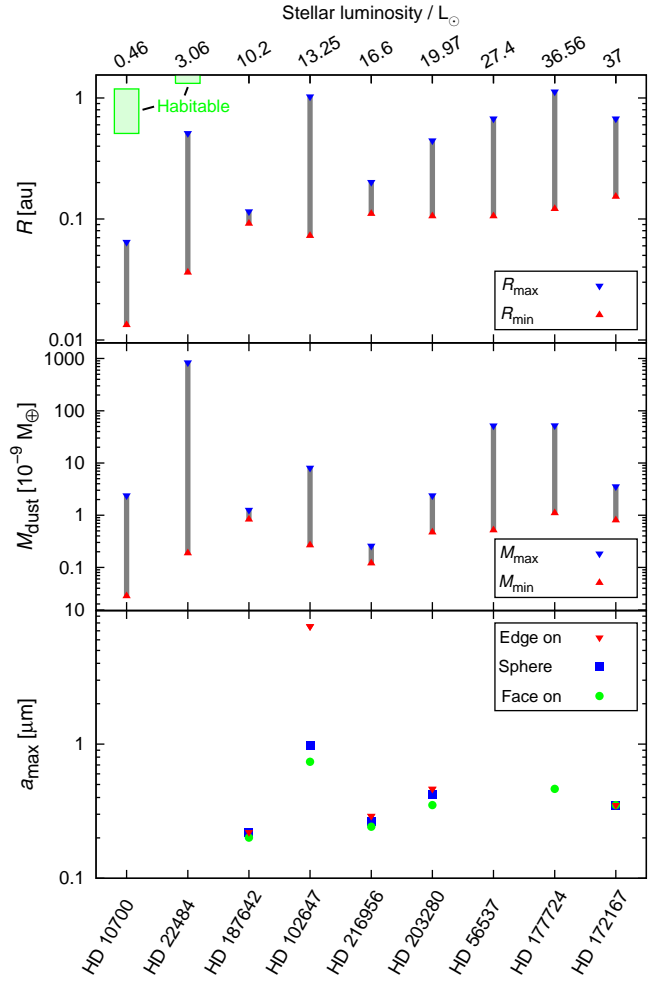


Figure 7. Results of the disc modelling of the Group I-targets (Tab. 1). The stellar luminosity increases from left to right. *Top:* Minimum and maximum disc ring radius, R_{\min} and R_{\max} , within which the hot zodiacal dust is located. An approximate habitable zone between 210 and 320 K is marked for HD 10700 and HD 22484 as green boxes. For the other systems, the corresponding habitable zone is outside of the displayed radii. *Middle:* Minimum and maximum dust mass, M_{\min} and M_{\max} , respectively. *Bottom:* Maximum grain size for discs with face-on or edge-on orientation and for the spherical shell.

HD 22484 only, the best fit for the remaining eight systems is $R_{\max} \propto L_*^{0.7 \pm 0.5}$.

Since we are interested in the most likely distance at which the hot dust is located, we may also choose to analyse the geometrical mean of the minimum and maximum radii, i.e. $R_{\text{mean}} = \sqrt{R_{\min} R_{\max}}$ instead of R_{\max} . Doing this without the outlier HD 22484 leads to an even flatter dependence, $R_{\text{mean}} \propto L_*^{0.6 \pm 0.2}$. In fact, the dust location may scale as the square root of the stellar luminosity, which would imply that all exozodiacal dust discs have approximately the same temperature. If true, this could mean that the hot dust location is driven by temperature-dependent processes. Alternatively, this may be a chance coincidence. For instance, if the hot dust is trapped by stellar magnetic fields (see Sect. 4), a similar trend may possibly arise if the Lorentz force scales with the stellar luminosity in a similar way. On any account,

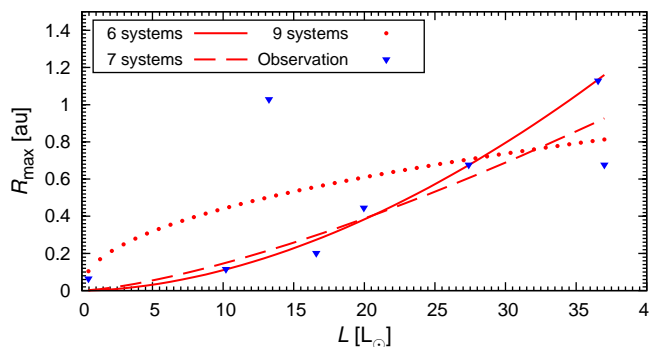


Figure 8. Maximum disc ring radius R_{\max} as a function of stellar luminosity L_* for the nine Group I-targets (blue triangles), fitted with a function $R_{\max} = c_1 L_*^{c_2}$. Excluding no system, or excluding HD 22484 and HD 102647, or excluding HD 22484, HD 102647 and Vega, the result is $R_{\max} \propto L_*^{0.5 \pm 0.3}$ (dots), $R_{\max} \propto L_*^{1.4 \pm 0.4}$ (dashed line), and $R_{\max} \propto L_*^{1.8 \pm 0.2}$ (solid line), respectively.

no definite conclusions can be made, given a small sample size and rather large uncertainties with which the dust ring radii are estimated.

In addition, we note that for all systems the location of the habitable zone defined in Sect. 2.5 is outside of the location of the hot dust.

The range of grain sizes depends on whether the sublimation radius is resolved by the observation at $\lambda = 8.5 \mu\text{m}$ or not (HD 10700, HD 22484, HD 56537). If it is not, we are not able to put any constraints on the particle size. Since larger dust grains are not excluded in these systems, scattered radiation has a higher impact on the NIR flux. HD 102647 and HD 177724 are marginally resolved by the MIR observation, resulting in a large maximum grain radius a_{\max} for at least one of the three disc geometries. For the remaining systems of Group I, the maximum grain sizes are constrained to be between $0.2 \mu\text{m}$ and $0.5 \mu\text{m}$ and the deviations for different disc inclinations are below 10%. Thermal reemission is the dominating source of the excess in the NIR. Consequently, the polarisation degree is below 5%, and for grain sizes below $\sim 0.2 \mu\text{m}$ even below 1%. The ratio of the scattered to total radiation amounts to values up to 35%. However, the modelling results in a lower limit of the minimum particle size for the systems HD 10700, HD 187642 and HD 216956.

The maximum dust mass M_{\max} shows the same behaviour as the maximum disc ring radius R_{\max} and is in the range $(0.26 - 840) \times 10^{-9} M_{\oplus}$, while the minimum dust mass M_{\min} amounts to $(0.03 - 1.1) \times 10^{-9} M_{\oplus}$. Again, the maximum dust masses can be much better constrained for the systems where the sublimation radius is spatially resolved by the MIR observation. In such systems, the maximum dust mass amounts to $(0.2 - 3.5) \times 10^{-9} M_{\oplus}$.

A decay of the dust mass with the stellar age is a robust theoretical prediction for “classical” debris discs, i.e., Kuiper-belt analogues (e.g. Dominik & Decin 2003; Wyatt et al. 2007b; Löhne et al. 2008). This trend has also been confirmed observationally, especially for A-type stars (e.g. Rieke et al. 2005; Su et al. 2006), although the dependence is much weaker for solar-type stars (e.g. Eiroa et al. 2013; Montesinos et al. 2016). However, it is not known whether the same is true for exozodiacal dust systems. To check this, we plotted the inferred minimum and maximum dust masses

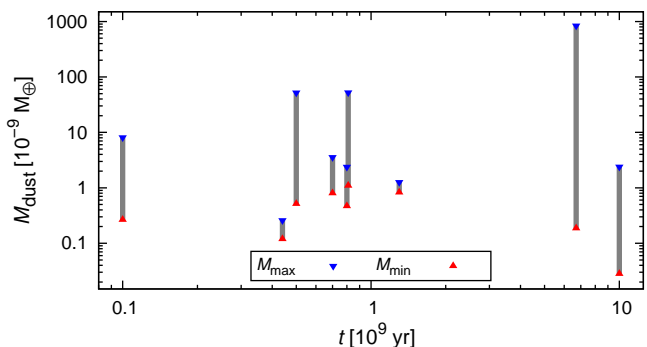


Figure 9. Minimum and maximum dust mass as a function of stellar age for the Group I-targets (Tab. 1).

as a function of stellar age in Figure 9. With the Pearson correlation coefficient $R_p = 0.29$ and the Spearman rank coefficient $R_s = 0.11$ (neglecting of HD 22484 and HD 102647: $R_p = -0.10$, $R_s = 0.04$), no strong correlation exists between the maximum mass of the hot exozodiacal dust and the age of the system.

3.3 Individual targets of Group I

In this section, individual sources of Group I are discussed briefly.

HD 10700 (τ Cet)

HD 10700 is one of the brightest sun-like stars in our neighbourhood (G8V, $K = 1.7^{\text{mag}}$) and with $\sim 10^{10}$ yr the oldest of the sample. The K band excess was first reported by Di Folco et al. (2007). While there is no significant excess at $\lambda = 8.5 \mu\text{m}$ or $24 \mu\text{m}$, Habing et al. (2001) reported excess at $60 \mu\text{m}$ and $100 \mu\text{m}$ and Greaves et al. (2004) and Lawler et al. (2014) presented resolved images at $70 \mu\text{m}$, $160 \mu\text{m}$ and $850 \mu\text{m}$.

We find that the hot dust has to be located between 0.013 au and 0.06 au . The minimum dust mass is about $0.03 \times 10^{-9} M_{\oplus}$. The maximum dust mass takes values from $1.2 \times 10^{-9} M_{\oplus}$ (face-on) to $2.4 \times 10^{-9} M_{\oplus}$ (edge-on). Since the sublimation radius of the large particles is resolved for the NIR observation but not for the MIR observation, the maximum grain size is not constrained. Particles smaller than $1 \mu\text{m}$ sublimate at larger distances than larger particles. For the face-on disc and the spherical dust sphere of HD 10700, this condition sets a lower limit for the grain sizes (see Fig. 10), and the minimum particle radius is 34 nm and 22 nm , respectively.

HD 22484 (10 Tau)

Kóspál et al. (2009) showed that the SED exhibits an excess at $70 \mu\text{m}$ for HD 22484, while there is no significant excess at $24 \mu\text{m}$. The ratio of the measured NIR flux to the flux at $8.5 \mu\text{m}$ is relatively small (~ 3.5).

The scattered radiation contributes to the NIR flux up to $\sim 30\%$ (for grains between $0.1 \mu\text{m}$ and $1 \mu\text{m}$), even though thermal reemission is the dominant source for the NIR flux at a wide range of the suitable parameter settings. The disc ring radii are not strongly affected by the disc inclination

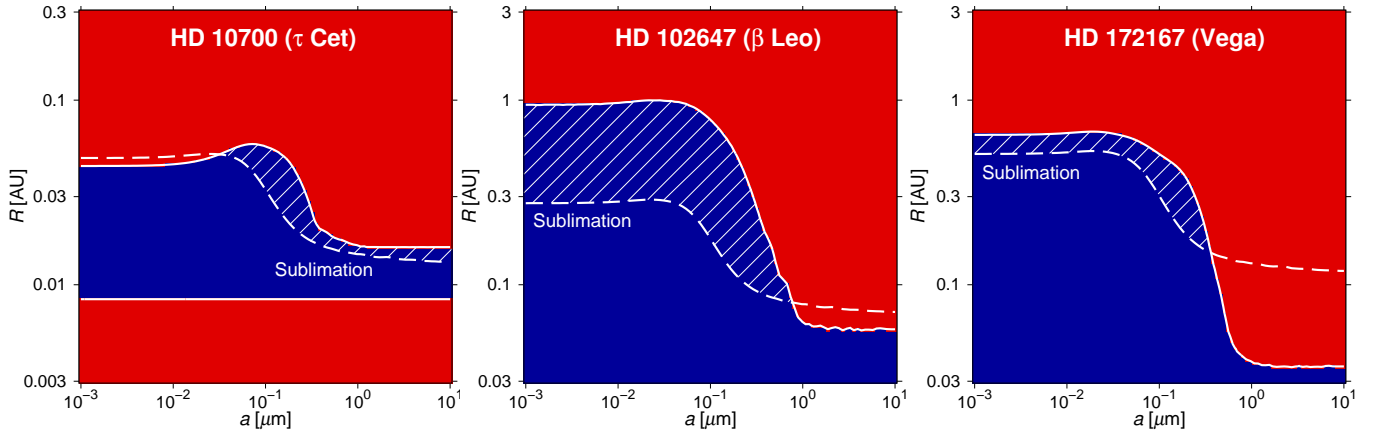


Figure 10. Same as Figure 4, but for the systems HD 10700 (τ Cet), HD 102647 (β Leo), and HD 172167 (Vega), and only for the face-on case. The dust material is pure graphite. For HD 10700, the sublimation radius and the upper blue-red border constrain the minimum dust grain size, while for HD 102647 and HD 172167 the maximum grain radii are constrained. HD 102647 is the only system of the sample with a significant excess at $8.5\,\mu\text{m}$ (Mennesson et al. 2014).

and take values between 0.035 au and 0.52 au. The minimum dust mass is about $0.2 \times 10^{-9} M_{\oplus}$ and the maximum dust mass is in the range $(150 - 840) \times 10^{-9} M_{\oplus}$. The grain sizes are not constrained.

HD 56537 (λ Gem)

The system was discussed in detail in Section 3.1. Besides the K band excess, there was no significant signal above the photosphere at $8.5\,\mu\text{m}$, $24\,\mu\text{m}$ or $70\,\mu\text{m}$ (Gáspár et al. 2013; Chen et al. 2014; Mennesson et al. 2014).

HD 102647 (β Leo, Denebola)

The K band excess of HD 102647 was first reported by Akeson et al. (2009). It is the only system of the sample with a significant excess at $8.5\,\mu\text{m}$ (Mennesson et al. 2014). HD 102647 also has a significant excess at both $24\,\mu\text{m}$ and $70\,\mu\text{m}$ (Su et al. 2006) and is well studied (e.g. Stock et al. 2010; Churcher et al. 2011), revealing a relative compact disc at $60 - 70$ au and with further dust components located close to 2 au to the star. Herschel images show a nearly face-on disc (Matthews et al. 2010).

In our disc modelling we derived the location of the hot exozodiacal dust to be between 0.07 au and 1 au. The minimum dust mass amounts to $0.3 \times 10^{-9} M_{\oplus}$. The maximum dust mass takes values from $5.8 \times 10^{-9} M_{\oplus}$ (face-on) to $8.1 \times 10^{-9} M_{\oplus}$ (edge-on). Since the sublimation radius is resolved for all particle sizes by the NIR and also marginally by the MIR observation, the maximum grain size is constrained to $0.74\,\mu\text{m}$ (face-on, Fig. 10), $7.6\,\mu\text{m}$ (edge-on) and $1.0\,\mu\text{m}$ (sphere).

HD 172167 (α Lyr, Vega)

HD 172167 shows excess in H band (Defrère et al. 2011) and K band (Absil et al. 2006), while the flux at $8.5\,\mu\text{m}$ is not significant but only slightly below the significance limit (Mennesson et al. 2014). Su et al. (2006) reported a large excess at $70\,\mu\text{m}$, which corresponds to a disc nearly face-on (Monnier et al. 2012). Vega is a rapid rotator (Peterson

et al. 2006) which makes stellar parameters a function of the stellar latitude. Consequently, the luminosity at the equator and at the poles derived from equatorial and polar values of the stellar radius R_{\star} and temperature T_{\star} deviate between $7900 - 10150$ K and $28 - 57 L_{\odot}$, respectively (Aufdenberg et al. 2006). In our simulations, we adopt intermediate values of $T_{\star} = 9620$ K and $37 L_{\odot}$ (Müller et al. 2010).

We find that the dust has to be located between 0.15 au and 0.68 au and the dust mass amounts to $(0.8 - 3.6) \times 10^{-9} M_{\oplus}$. The sublimation radius is resolved for all particle sizes by both the NIR and the MIR observation. Consequently, the maximum grain size is well constrained ($< 0.35\,\mu\text{m}$, Fig. 10). These values are comparable to the parameters found by Absil et al. (2006) and Defrère et al. (2011), who indicated grains of sizes smaller than $0.2\,\mu\text{m}$ and distances of $R \sim 0.2 - 0.3$ au.

HD 177724 (ζ Cep), HD 187642 (α Aql, Altair), and HD 203280 (α Cep, Alderamin)

These three systems are all showing an excess in the K band but are free of excess at any longer wavelengths (Habing et al. 2001; Chen et al. 2005; Plavchan et al. 2009; Gáspár et al. 2013; Mennesson et al. 2014).

For HD 177724, the minimum and maximum of the inner disc ring radius amount to about 0.12 au and 1.1 au, respectively. The minimum mass is between $1.1 \times 10^{-9} M_{\oplus}$ and $1.3 \times 10^{-9} M_{\oplus}$ and the maximum mass lies between $10 \times 10^{-9} M_{\oplus}$ and $52 \times 10^{-9} M_{\oplus}$. For the edge-on case and the spherical dust shell, the sublimation radius is unresolved for the large dust grains, and thus the maximum dust grain size not constrained. For the face-on case, the maximum grain size amounts to $0.46\,\mu\text{m}$.

For HD 187644, the dust is strongly confined to a range between 0.09 au and 0.11 au and the mass amounts to $(0.8 - 1.3) \times 10^{-9} M_{\oplus}$. The minimum grain size is about $0.15\,\mu\text{m}$ and the maximum grain size amounts to $0.22\,\mu\text{m}$.

For HD 203280, the inner dust ring radius is located between 0.1 au and 0.45 au with a dust mass of $(0.47 - 2.4) \times 10^{-9} M_{\oplus}$. The maximum grain size is constrained to $0.35\,\mu\text{m}$ (face-on), $0.46\,\mu\text{m}$ (edge-on) and $0.42\,\mu\text{m}$ (sphere).

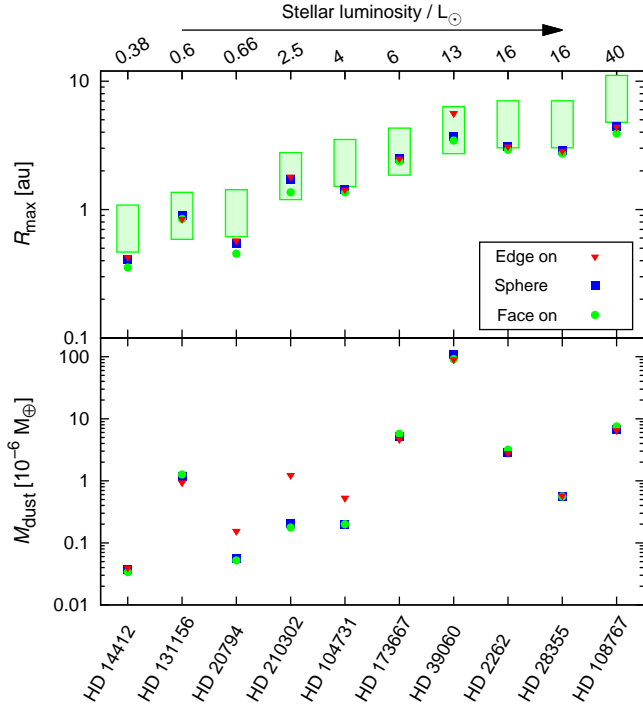


Figure 11. Results of the disc modelling of the Group II-targets (Tab. 1) for discs with face-on or edge-on orientation and for the spherical shell. The stellar luminosity increases from left to right. *Top:* Maximum disc ring radius R_{\max} , within which the hot zodiacal dust is located. Approximate habitable zones between 210 and 320 K are marked as green boxes for each system. *Bottom:* Maximum dust mass.

HD 216956 (α PsA, Fomalhaut)

The well-studied debris disc system of Fomalhaut shows excess in K band (Absil et al. 2009), while the excess at $8.5\mu\text{m}$ is not significant (Mennesson et al. 2014). At slightly longer wavelengths, an unresolved emission was detected with Spitzer/IRS which is interpreted as warm dust (Stapelfeldt et al. 2004; Su et al. 2013). At $70\mu\text{m}$ and $850\mu\text{m}$ a large excess is observed which is assigned to reemission of the cold debris belt at 140 au (Acke et al. 2012; Boley et al. 2012).

In our disc modelling we derived the minimum and maximum disc ring radii of the hot exozodiacal dust to 0.11 au and 0.2 au, respectively. The dust mass amounts to $(0.12 - 0.26) \times 10^{-9} M_{\oplus}$ and the minimum grain size to $0.1\mu\text{m}$. Since the sublimation radius is resolved for all particle sizes by both the NIR and the MIR observation, the maximum grain size is constrained to $0.24\mu\text{m}$ (face-on), $0.29\mu\text{m}$ (edge-on) and $0.27\mu\text{m}$ (sphere). These values are comparable to the parameters found in the modelling of Lebreton et al. (2013), where $a < 0.5\mu\text{m}$ and $R \sim 0.1 - 0.3$ au.

3.4 Survey: Group II-targets

Targets of Group II are those systems with a circumstellar NIR excess for which no interferometric observations at wavelengths $\lambda = 8.5\mu\text{m}$ exist. We performed the calculations of the SED also for each target of Group II and determined

the parameter settings which reproduce the observational data. The results are shown in Figure 11.

The grain size could not be constrained for any system of Group II, i.e. grain sizes from 1 nm to $100\mu\text{m}$ all reproduce the observed NIR excess without overestimating fluxes in the MIR or FIR.

The maximum ring radii R_{\max} which are in agreement with the observational constraints amount to values between 0.3 au and 6 au, i.e. they are a factor of six larger than in the case of Group I-targets. As a result, in five of the ten systems dust is potentially located in the habitable zone (while in the other five it is close to the inner edge of that zone). The dust masses amount to up to $1 \times 10^{-4} M_{\oplus}$ and are thus more than two magnitudes larger than the dust masses of the Group I-targets. Of course, this does not mean that the hot discs of Group II are more massive and larger than the discs of Group I. The only reason for the difference is that interferometric observations around $\sim 10\mu\text{m}$, available for the Group I, constrain the disc parameters much more tightly.

Similar to the Group I-targets, the maximum disc ring radius R_{\max} seems to increase with increasing stellar luminosity. Only HD 39060 (β Pic) contradicts to this trend, for which a large disc ring radius up to ~ 6 au is inferred. This is a consequence of large MIR and FIR fluxes above the stellar photosphere, which are caused by dust at larger radii of the massive disc around β Pic. Moreover, β Pic with an age of 23 ± 3 Myr (Mamajek & Bell 2014) may still be in the process of planet formation, especially in the inner 10 au of the disc. Thus, the observed NIR excess could be related to the end of the planet building phase rather than to exozodiacal dust (Absil et al. 2008).

The Pearson and the Spearman rank correlation coefficients between $\log L_{\star}$ and $\log R_{\max}$ of all targets of Group II amount $R_p = 0.94$ and $R_s = 0.91$, respectively (neglecting β Pic: $R_p = 0.97$ and $R_s = 0.96$), indicating a significant trend. Nevertheless, it should be noted that for the Group II-targets only the observed fluxes at $\lambda = 24\mu\text{m}$ and $70\mu\text{m}$ are used which are not cleaned by the contribution of the stellar photosphere (Sect. 2.4), so the derived correlation between $\log L_{\star}$ and $\log R_{\max}$ could be caused by the contribution of the stellar photosphere rather than by the emission of the dust.

While the weak dust emission on top of the bright stellar emission at wavelengths around $\sim 10\mu\text{m}$ is difficult to deduce from the photometry, interferometric observations provide a direct estimation of the flux ratio between the circumstellar environment and the photosphere of the star. Well determined fluxes at these wavelengths are necessary to find better constraints for the parameters of the hot exozodiacal dust. Therefore, high resolution interferometric observations around $\sim 10\mu\text{m}$ of the Group II-targets are required. HD 108767 and HD 173667 will be targets of the planned survey “Hunt for Observable Signatures of Terrestrial planetary Systems (HOSTS)” on the Large Binocular Telescope Interferometer (Weinberger et al. 2015), observing in the N’ band ($\lambda = 9.8 - 12.4\mu\text{m}$).

3.5 Uncertainty of the NIR excess

This study intends to put general constraints on the hot dust, based on the observational data available. An essen-

tial source of information is the NIR data. However, the NIR excess measurements have large 1σ -uncertainties, typically between 10% and 30%. Thus it is important to check how the constraints we derive would change if the actual NIR flux were larger or smaller by 1σ than the nominal value.

We do this again for the exemplary system HD 56537, for which the NIR flux is $27 \text{ mJy} \pm 5.8 \text{ mJy}$. The uncertainty of this flux measurement is 21%. Assuming the flux is increased (decreased) by 1σ results in a decreasing (increasing) of the maximum disc ring radius of 20% for the three disc inclinations. Since the sublimation radius is still the minimum disc ring radius, R_{min} and the dust masses are unaltered.

3.6 Variability of the NIR excess

Using VLTI/PIONIER in H band, [Ertel et al. \(2016\)](#) performed follow-up observations for seven Group II-targets. They concluded that the phenomenon responsible for the excesses persists for the majority of the systems for the explored time scales of at least two to four years. Six of the seven systems show no significant variation, while HD 7788 is the first strong candidate for variability. Therefore, HD 7788 was excluded from our study.

For the three remaining targets of Group II as well as for the complete Group I no follow-up observations exist yet, and no specific statements can be made concerning the variability of the excess of these individual targets. However, considering the fact that [Ertel et al. \(2016\)](#) found at least one of seven systems to show significant variability, the assumption of a temporal constant NIR excess in our study might not hold for all our targets. As shown in Section 3.5, this might have extensive influence on the dust parameters derived for these individual systems. For example, if we assumed the NIR excess of HD 56537 to be by a factor of 2 lower, the maximum disc ring radius would increase by a factor of 1.9. Only further follow-up observations can reveal time variability or constancy of the excess in these systems.

Besides the stability of the NIR detections over at least a few years, it is still unclear if the hot dust exists for longer than ten years. [Ertel et al. \(2014\)](#) found a detection rate of hot exozodiacal dust in the H band of 11%, so if the dust has lifetimes below ten years, it has to be replenished in time intervals smaller than ~ 100 years. As long as the formation mechanisms of the hot dust are unknown, this can be clarified again only by follow-up observations over a longer period. If the phenomenon responsible for the excesses is stable for time scales of ten to twenty years, it is highly probable that the excess of most systems already existed in the past when they were observed with Spitzer, which has been up to eight years before the NIR observations. If this is not the case, new observations in the MIR would be necessary to clarify if the phenomenon responsible for the NIR excess causes significant excess at wavelengths beyond $20 \mu\text{m}$. This would influence primarily the results of the Group II-targets, since the modelling parameters of these targets are constrained by the Spitzer observations, while the results of the Group I-targets are mainly constrained by the interferometric observations at $\lambda = 8.5 \mu\text{m}$, which have been taken up to four years before the NIR observations.

In summary, only follow-up and quasi-simultaneous

multi-wavelength observations can clarify the time variability or stability of the hot dust phenomenon.

3.7 Spectrally dispersed data

The PIONIER data come from three spectral channels across the H band ($\lambda = 1.59 \mu\text{m}, 1.68 \mu\text{m}, 1.77 \mu\text{m}$) which allows one to investigate the spectral slope of the excess of Group II-targets. These spectrally dispersed data may allow one to put further constraints on the location and the sizes of the dust grains, though the significance of the slopes is quite small ([Defrère et al. 2012](#); [Ertel et al. 2014](#)).

We apply the fitted slopes a_{slope} and their uncertainties σ_{slope} as derived by [Ertel et al. \(2014\)](#). Among all the systems of Group II, HD 108767 has the smallest uncertainty with $\sigma_{\text{slope}} = 1.35$. For each parameter setting in Table 2, we calculate the fluxes at $\lambda = 1.59 \mu\text{m}$ and $1.77 \mu\text{m}$ for HD 108767 and determine the spectral slope of the simulated data. As suggested by [Ertel et al. \(2014\)](#), a $3\sigma_{\text{slope}}$ criterion is used to prove if the measured slope coincides with the simulated slopes within the uncertainties.

Unfortunately, the spectrally dispersed data could not further constrain the parameters. Almost the entire parameter space considered would yield spectral slopes in the H band which are consistent within the uncertainties with the simulated slopes ($a_{\text{slope}} \in [-2.58, 5.52]$). In particular, the suitable parameter settings as derived from the sublimation radius and the ratio of NIR to MIR fluxes result in slopes below 5. Stronger constraints from the spectral slope require data of higher precision or over a wider wavelength range to minimise the uncertainties of the slopes (e.g. using VLTI/MATISSE).

4 DISCUSSION

Our disc modelling shows that grains have to be absorbing (e.g. composed of graphite), have to be located within 1 au, and have to be smaller than $0.5 \mu\text{m}$ in radius (at least for systems with spatially resolved sublimation radius in the MIR). However, the disc models presented here only show which properties the dust must have to reproduce the observational data, without addressing the physical mechanisms responsible for the production and evolution of that dust in the system.

Explaining the presence of small grains in significant amounts close to the star poses a challenge (e.g. [Matthews et al. 2014](#)). If this dust was produced in a steady-state collisional cascade operating in an asteroid belt analogue, such a belt would rapidly deplete. The resulting dust fractional luminosities would be several orders below the observed ones, at least in Gyr-old systems (e.g. [Wyatt et al. 2007a](#); [Löhne et al. 2008](#); [Ertel et al. 2014](#)).

An additional problem arises from the fact that the dust grains are inferred to be small enough to be either swiftly expelled from the system by direct radiation pressure or to undergo a rapid inward drift to the sublimation region by the Poynting-Robertson force. The radiation blow-out and Poynting-Robertson timescale ([Burns et al. 1979](#)) of $1 \mu\text{m}$ sized grains at 1 au is on the order of $\sim 10^3$ years for the lowest luminosity star of the sample ($L_{\star} = 0.46 L_{\odot}$) and even below $\sim 10^2$ years for the highest luminosity star ($L_{\star} =$

$37 L_{\odot}$). If a local dust production in a steady-state regime is assumed, these short timescales will imply unrealistically high dust replenishment rates.

In view of these difficulties, alternative scenarios have been proposed. These include transient dynamical events similar to the late heavy bombardment in the solar system (Wyatt et al. 2007a; Kennedy & Wyatt 2013), the sublimation of a “supercomet” close to the star (Beichman et al. 2005), or the aftermath of a large collision (Lisse et al. 2008, 2009; Jackson et al. 2014). However, these scenarios either fail to explain the presence of exozodiacal dust around old stars or have a low probability, which is incompatible with the observed frequency of systems with hot dust. Another scenario is the delivery of material from exterior debris belts to the star’s vicinity, e.g. by comets dynamically perturbed from the outer cold discs, planetesimals or planets and disintegrating in the inner system (e.g. Faramaz et al. 2017). However, this scenario suffers from a number of rather unconstrained parameters such as unknown number and parameters of scattering planets and unknown efficiency of comet disintegration (Bonsor et al. 2012, 2013b). Yet another possibility, an inward drift of dust grains by the Poynting-Robertson drag with subsequent grain sublimation, would predict a much higher flux in the MIR than is actually observed (Kobayashi et al. 2009, 2011).

Currently, the most promising model is that of charged, nano-scale dust grains which are trapped in the stellar magnetic field through the Lorentz force (Czechowski & Mann 2010; Su et al. 2013; Rieke et al. 2016). Such a model can be further improved by including a more realistic sublimation physics for dust grains (Lebreton et al. 2013). For example, MgO, FeO and C nano-grains have melting temperatures larger than 3000 K, allowing grains of these or composite materials to survive closer to the star. Nano-particles can be charged through the photoelectric effect (for early-type stars) or stellar wind (for late-type stars; Pedersen & Gómez de Castro 2011). With the assumption of surface fields similar to the Sun (~ 1 G), the magnetic fields will then be able to cage the nano-grains in the systems, causing the measured NIR fluxes.

5 CONCLUSIONS

Based on near- to far-infrared observations of a sample of nine systems harbouring hot exozodiacal dust, we derived the following constraints on the dust properties and dust distribution in the vicinity of these stars:

- The observed fluxes in the NIR and at a wavelength of $\lambda = 8.5 \mu\text{m}$ are inconsistent with dust compositions dominated by silicate material. Instead, carbonaceous materials such as graphite are compatible with the observations.
- The maximum disc ring radius R_{max} amounts to 0.06 au to 1 au. We find evidence for R_{max} to increase with the stellar luminosity L_* . It is possible, albeit unsure, that R_{max} scales as a square root of L_* , which would imply a nearly constant temperature of hot dust in all the systems studied.
- The maximum grain radius is constrained to 0.2–0.5 μm for systems for which the sublimation radius is spatially resolved by the interferometric MIR observation. If it is not, the particle size is not or poorly constrained by our study.

The result is independent of whether the observed interferometric MIR flux is significant or not.

- For some of these systems, we are also able to constrain the minimum grain size. To be consistent with the observed fluxes and to lie outside the sublimation distance, the dust grains have to be larger than 20 – 150 nm in radius.
- The dust masses in the systems are derived to range between $0.2 \times 10^{-9} M_{\oplus}$ and $3.5 \times 10^{-9} M_{\oplus}$ for systems for which the sublimation radius is spatially resolved by the interferometric MIR observation. If it is not, the masses range between $0.26 \times 10^{-9} M_{\oplus}$ and $840 \times 10^{-9} M_{\oplus}$. There is no obvious correlation between the dust mass and the age of the system.
- Thermal reemission is the dominant source of the excess not only in the MIR and FIR, but also in the NIR. Nevertheless, for systems whose sublimation radius is not spatially resolved by the interferometric MIR observation, a contribution of scattered light of up to 35% cannot be completely excluded.
- The polarisation degree of the NIR radiation of the dust is below 5% for all systems, and for grains smaller than 0.2 μm even below 1%. This finding is consistent with recently published polarisation observations.

We also modelled another ten systems known to harbour exozodiacal dust, for which $\lambda = 8.5 \mu\text{m}$ data are not available. The results for these systems appear similar, albeit with weaker constraints on the grain size, dust location, and dust masses.

The origin of the exozodiacal dust is still a matter of debate. Models that consider charged nano-grains trapped in stellar magnetic fields, combined with a proper choice of materials and realistic sublimation physics, can yield a satisfactory explanation for the existence of the exozodiacal dust. The results of this paper pose tighter constraints on the hot dust material and may help improve and verify such models.

ACKNOWLEDGEMENTS

The authors thank the DFG for financial support under contracts WO 857/13-1, WO 857/15-1, KR 2164/15-1, and HM 1164/9-1. We also thank Bertrand Mennesson for useful information on the fluxes of interferometric nulling data and the anonymous referee for a precious help in improving the quality of the paper.

REFERENCES

- Absil O., et al., 2006, *A&A*, **452**, 237
 Absil O., et al., 2008, *A&A*, **487**, 1041
 Absil O., Mennesson B., Le Bouquin J.-B., Di Folco E., Kervella P., Augereau J.-C., 2009, *ApJ*, **704**, 150
 Absil O., et al., 2013, *A&A*, **555**, A104
 Acke B., et al., 2012, *A&A*, **540**, A125
 Agol E., 2007, *MNRAS*, **374**, 1271
 Akeson R. L., et al., 2009, *ApJ*, **691**, 1896
 Aufdenberg J. P., et al., 2006, *ApJ*, **645**, 664
 Backman D. E., Paresce F., 1993, in Levy E. H., Lunine J. I., eds, *Protostars and Planets III*. pp 1253–1304
 Beckwith S. V. W., 2008, *ApJ*, **684**, 1404
 Beichman C. A., et al., 2005, *ApJ*, **626**, 1061

- Beichman C. A., et al., 2006, *ApJ*, **652**, 1674
- Boley A. C., Payne M. J., Corder S., Dent W. R. F., Ford E. B., Shabram M., 2012, *ApJ*, **750**, L21
- Bonsor A., Augereau J.-C., Thébault P., 2012, *A&A*, **548**, A104
- Bonsor A., Kennedy G. M., Crepp J. R., Johnson J. A., Wyatt M. C., Sibthorpe B., Su K. Y. L., 2013a, *MNRAS*, **431**, 3025
- Bonsor A., Raymond S. N., Augereau J.-C., 2013b, *MNRAS*, **433**, 2938
- Boyajian T. S., et al., 2013, *ApJ*, **771**, 40
- Burns J. A., Lamy P. L., Soter S., 1979, *Icarus*, **40**, 1
- Chen C. H., et al., 2005, *ApJ*, **634**, 1372
- Chen C. H., et al., 2006, *ApJS*, **166**, 351
- Chen C. H., Mittal T., Kuchner M., Forrest W. J., Lisse C. M., Manoj P., Sargent B. A., Watson D. M., 2014, *ApJS*, **211**, 25
- Churcher L. J., et al., 2011, *MNRAS*, **417**, 1715
- Czechowski A., Mann I., 2010, *ApJ*, **714**, 89
- Defrère D., et al., 2011, *A&A*, **534**, A5
- Defrère D., et al., 2012, *A&A*, **546**, L9
- Di Folco E., Thévenin F., Kervella P., Domiciano de Souza A., Coudé du Foresto V., Ségransan D., Morel P., 2004, *A&A*, **426**, 601
- Di Folco E., et al., 2007, *A&A*, **475**, 243
- Dominik C., Decin G., 2003, *ApJ*, **598**, 626
- Dorschner J., Begemann B., Henning T., Jäger C., Mutschke H., 1995, *A&A*, **300**, 503
- Draine B. T., Malhotra S., 1993, *ApJ*, **414**, 632
- Eiroa C., et al., 2013, *A&A*, **555**, A11
- Ertel S., Wolf S., Metchev S., Schneider G., Carpenter J. M., Meyer M. R., Hillenbrand L. A., Silverstone M. D., 2011, *A&A*, **533**, A132
- Ertel S., et al., 2014, *A&A*, **570**, A128
- Ertel S., et al., 2016, *A&A*, **595**, A44
- Faramaz V., Ertel S., Booth M., Cuadra J., Simmonds C., 2017, *MNRAS*, **465**, 2352
- Fixsen D. J., Dwek E., 2002, *ApJ*, **578**, 1009
- Gáspár A., Rieke G. H., Balog Z., 2013, *ApJ*, **768**, 25
- Gillett F. C., 1986, in Israel F. P., ed., *Astrophysics and Space Science Library Vol. 124, Light on Dark Matter*. pp 61–69, doi:10.1007/978-94-009-4672-9_10
- Greaves J. S., Wyatt M. C., Holland W. S., Dent W. R. F., 2004, *MNRAS*, **351**, L54
- Habing H. J., et al., 2001, *A&A*, **365**, 545
- Hahn J. M., Zook H. A., Cooper B., Sunkara B., 2002, *Icarus*, **158**, 360
- Jackson A. P., Wyatt M. C., Bonsor A., Veras D., 2014, *MNRAS*, **440**, 3757
- Jäger C., Mutschke H., Henning T., 1998, *A&A*, **332**, 291
- Kennedy G. M., Wyatt M. C., 2013, *MNRAS*, **433**, 2334
- Kimura H., Mann I., 1998, *Earth, Planets, and Space*, **50**, 493
- Kobayashi H., Watanabe S.-i., Kimura H., Yamamoto T., 2009, *Icarus*, **201**, 395
- Kobayashi H., Kimura H., Watanabe S.-i., Yamamoto T., Müller S., 2011, *Earth, Planets, and Space*, **63**, 1067
- Kopparapu R. K., et al., 2013, *ApJ*, **765**, 131
- Kóspál Á., Ardila D. R., Moór A., Ábrahám P., 2009, *ApJ*, **700**, L73
- Krivov A. V., 2010, *Research in Astronomy and Astrophysics*, **10**, 383
- Lamoreaux R. H., Hildenbrand D. L., Brewer L., 1987, *Journal of Physical and Chemical Reference Data*, **16**, 419
- Lawler S. M., et al., 2014, *MNRAS*, **444**, 2665
- Lebreton J., et al., 2013, *A&A*, **555**, A146
- Leinert C., 1996, in Dwek E., ed., *American Institute of Physics Conference Series Vol. 348, American Institute of Physics Conference Series*. pp 53–63
- Lisse C. M., Chen C. H., Wyatt M. C., Morlok A., 2008, *ApJ*, **673**, 1106
- Lisse C. M., Chen C. H., Wyatt M. C., Morlok A., Song I., Bryden G., Sheehan P., 2009, *ApJ*, **701**, 2019
- Löhne T., Krivov A. V., Rodmann J., 2008, *ApJ*, **673**, 1123
- Mamajek E. E., 2012, *ApJ*, **754**, L20
- Mamajek E. E., Bell C. P. M., 2014, *MNRAS*, **445**, 2169
- Mann I., et al., 2004, *Space Sci. Rev.*, **110**, 269
- Marion L., et al., 2014, *A&A*, **570**, A127
- Marshall J. P., et al., 2016, *ApJ*, **825**, 124
- Matthews B. C., et al., 2010, *A&A*, **518**, L135
- Matthews B. C., Krivov A. V., Wyatt M. C., Bryden G., Eiroa C., 2014, *Protostars and Planets VI*, pp 521–544
- Mawet D., Mennesson B., Serabyn E., Stapelfeldt K., Absil O., 2011, *ApJ*, **738**, L12
- Mennesson B., et al., 2014, *ApJ*, **797**, 119
- Mie G., 1908, *Annalen der Physik*, **330**, 377
- Monnier J. D., et al., 2012, *ApJ*, **761**, L3
- Montesinos B., et al., 2016, *A&A*, **593**, A51
- Müller S., Löhne T., Krivov A. V., 2010, *ApJ*, **708**, 1728
- Nesvorný D., Jenniskens P., Levison H. F., Bottke W. F., Vokrouhlický D., Gounelle M., 2010, *ApJ*, **713**, 816
- Pace G., 2013, *A&A*, **551**, L8
- Pedersen A., Gómez de Castro A. I., 2011, *ApJ*, **740**, 77
- Pepe F., et al., 2011, *A&A*, **534**, A58
- Peterson D. M., et al., 2006, *Nature*, **440**, 896
- Plavchan P., Werner M. W., Chen C. H., Stapelfeldt K. R., Su K. Y. L., Stauffer J. R., Song I., 2009, *ApJ*, **698**, 1068
- Rieke G. H., et al., 2005, *ApJ*, **620**, 1010
- Rieke G. H., Gáspár A., Ballering N. P., 2016, *ApJ*, **816**, 50
- Roberge A., et al., 2012, *PASP*, **124**, 799
- Stapelfeldt K. R., et al., 2004, *ApJS*, **154**, 458
- Stock N. D., et al., 2010, *ApJ*, **724**, 1238
- Su K. Y. L., et al., 2006, *ApJ*, **653**, 675
- Su K. Y. L., et al., 2013, *ApJ*, **763**, 118
- Trilling D. E., et al., 2008, *ApJ*, **674**, 1086
- Vican L., 2012, *ApJ*, **143**, 135
- Vitense C., Krivov A. V., Kobayashi H., Löhne T., 2012, *A&A*, **540**, A30
- VizieR, VizieR photometry viewer, <http://vizier.u-strasbg.fr/vizier/sed/>
- Weinberger A. J., et al., 2015, *ApJS*, **216**, 24
- Weingartner J. C., Draine B. T., 2001, *ApJ*, **548**, 296
- Wolf S., Voshchinnikov N. V., 2004, *Computer Physics Communications*, **162**, 113
- Wyatt M. C., 2008, *ARA&A*, **46**, 339
- Wyatt M. C., Smith R., Greaves J. S., Beichman C. A., Bryden G., Lisse C. M., 2007a, *ApJ*, **658**, 569
- Wyatt M. C., Smith R., Su K. Y. L., Rieke G. H., Greaves J. S., Beichman C. A., Bryden G., 2007b, *ApJ*, **663**, 365
- Wyatt M. C., et al., 2012, *MNRAS*, **424**, 1206
- Zeidler S., Posch T., Mutschke H., Richter H., Wehrhan O., 2011, *A&A*, **526**, A68
- Zeidler S., Mutschke H., Posch T., 2015, *ApJ*, **798**, 125
- Zorec J., Royer F., 2012, *A&A*, **537**, A120
- van Belle G. T., Ciardi D. R., Thompson R. R., Akeson R. L., Lada E. A., 2001, *ApJ*, **559**, 1155
- van Belle G. T., et al., 2006, *ApJ*, **637**, 494
- van Leeuwen F., 2007, *A&A*, **474**, 653
- van Lieshout R., Dominik C., Kama M., Min M., 2014, *A&A*, **571**, A51

This paper has been typeset from a \LaTeX file prepared by the author.